International Journal of Engineering and Technical Research (IJETR)
ISSN: 2321-0869 (O) 2454-4698 (P), Volume-7, Issue-2, February 2017

Structural design points in arrayed micro thermal sensors (I) ~ silicon-based approach ~

Hirofumi Miki, S. Tsuchitani

***Abstract*— Generally, silicon micro machining technology was used in the fabrication of micro thermal sensors, due to the possibility of integration with IC on the same sensor chip, and its well-established know-hows. However, particular attention is necessary due to its features of high thermal conductivity and mechanical brittleness. In this paper, the design points in the applicable structure of arrayed micro thermal sensor are discussed in detail by means of simulation analysis combine with the fabrication process technology.**

***Index Terms*— MEMS, thermal sensor, array sensor, fingerprint capture, structural design**

I. INTRODUCTION

Micro thermal sensors have been widely used in the application of temperature or flow sensing and it is also possible even in the application of fingerprint pattern capture. Generally, silicon micro machining was used in the fabrication of these sensors, due to the possibility of integration with IC on the same sensor chip, and its well-established technology. However, particular attention is necessary because silicon possesses features of high thermal conductivity and mechanical brittleness. Here, silicon micro machining technology is need to be briefly introduced first. Silicon micro machining can be divided into following two categories: bulk and surface micromachining.

In bulk micromachining, the wet and dry silicon etching techniques is used employing etch masks and etch stops to sculpt mechanical devices from a silicon wafer. The mixture of hydrofluoric acid, nitric acid and acetic acid (HNA) is an isotropic silicon etchant with silicon nitride as the etch mask. Certain other chemicals, such as ethylene-diamine-pyrocatechol with water (EDP or EPW), tetramethyl ammonium hydroxide (TMAH), hydrazine solution and potassium hydroxide (KOH) solution are anisotropic silicon etchants with silicon dioxide or silicon nitride as the etch mask. Anisotropic etchant etches silicon much faster in (100) and (110) crystallographic directions than the (111) direction, which allows the design of microstructures to be naturally bounded by {111} crystalline planes. The vertical etch stop can be (a) a heavily boron-doped layer buried under the epitaxial layer, (b) silicon dioxide in SOI wafers, and (c) p-n junction (for electrochemical etching). It is generally agreed that silicon bulk micromachining using wet chemical etching is a mature technology and many silicon microstructures including beams, diaphragms, nozzles, etc. have been made. These microstructures have formed the building blocks of many MEMS devices. Nevertheless, there are some disadvantages for bulk micromachining using wet anisotropic etching. For example, the geometry that can be made is generally limited by the silicon crystalline orientations; bulky corner compensation structures are often needed in order to make convex structures such as beams; the choices of etch mask are extremely limited. In contrast, dry etching processes do not have these problems and have recently attracted more attention. These include laser drilling, reactive ion etching (RIE), ion milling and even micro electro-discharge-machining (EDM). However, generally the equipment for dry etching process is expensive.

In surface micromachining, microstructures are fabricated on the surface of the silicon substrate by consecutive deposition and patterning of thin-film structural and sacrificial layers. The silicon substrate, however, only serves as a mechanical support and usually does not participate in the processing. At a certain stage, the sacrificial layers are removed by wet or dry etching that does not attack the structural layers. Silicon dioxide is the most often used sacrificial material, while polysilicon and some metals are occasionally used as sacrificial materials. The most common structural materials are polysilicon and silicon nitride. The dimensions of surface micromachined structures are generally one or two order of magnitude smaller than those of bulk micromachined devices. One particular advantage of the surface micromachined devices is their easy integration with IC components, since the wafer surface is also the working area of IC elements [1].

II. STRUCTURAL DESIGN

A. Thermal isolation strucutures

In micro thermal sensor design, the most important aspects are sensitivity, response speed, and mechanical strength. As far as the sensitivity is concerned, the contribution of the sensing-information independent heat transfer (e.g., flow-independent heat transfer in flow sensor) should preferably be small. To achieve this, the sensing area must be thermally isolated from its supporting structure sufficiently. Figure 1 shows the easily achievable thermal isolation structures by silicon micromachining techniques. The simplest structure is formed by a closed membrane. In a square area in the center of the chip the major part of the silicon has been etched away from the back of the chip, leaving only a thin diaphragm at the surface with a thickness of typically a few microns. By etching away parts of the membrane surface as well, cantilever beams, bridges and suspended membranes can be formed. A number of silicon micromachined thermal sensors employing the basic structures have been reported: closed membrane [2-10], bridge

Hirofumi Miki, Dept. of Systems Engineering Wakayama University, 930, Sakaedani, Wakayama, Japan
S. Tsuchitani, Dept. of Systems Engineering Wakayama University,930, Sakaedani, Wakayama, Japan

[11-19], cantilever [20-23] and floating membrane [24-27]. However, all these are the examples of single element structures. To realize an array layout of these single elements, there are new thermal design issues compared to those of the single thermal sensors.

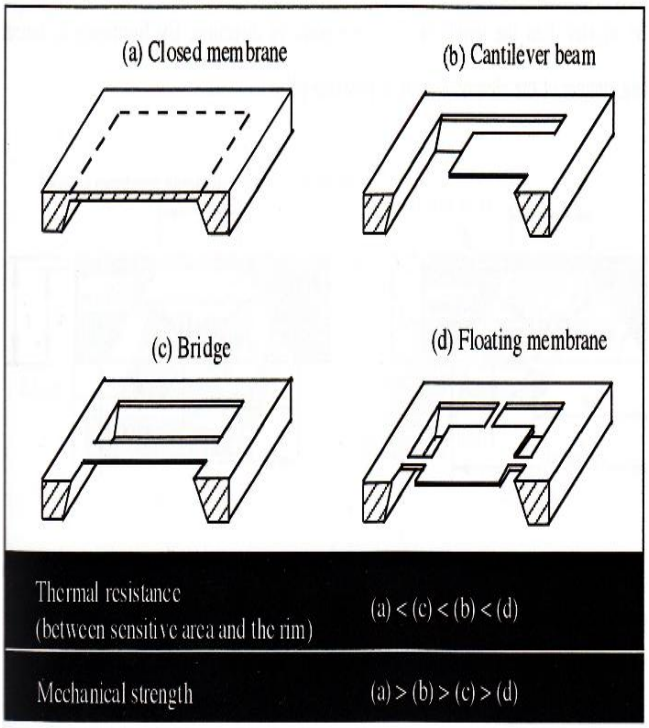

Fig. 1 Basic thermal structures that can be easily created by silicon micromachining: (a) Closed membrane, (b) Cantilever beam, (c) Bridge, and (d) Suspended floating membrane.

B. Previous research in arrayed structures

Bulk and surface micromachining technology has been employed to realize thermal sensor arrays [28-30, 32-40]. In bulk micromachining of anisotropic wet etching, the design freedom is limited by the crystallographic structure of the wafer resulting in limitations for the miniaturization of arrayed element size. When fabricate a thermal isolation diaphragm structure on a (100) silicon wafer (thickness: d) by backside anisotropic wet etching, there exists a length limit of $l_{min} = 2d(\cot 54.74°)$ due to the inclined walls given by the etch-stopping (111) planes as shown in Fig. 2. The size of the array cell should not be shorter than the length in the corresponding direction. By front-side undercut etching, denser of the elements array is possible [40]. Surface micromachining enables small structures and offers a high freedom of design, however, the maximum gap distance between the functional layers and the silicon substrate is typically only several μm [31]. Figure 3 shows one example of a surface micromachined element structure corresponding to 340×240 elements with an element size of 50×50-μm^2 for the fabrication of uncooled focal plane arrays [29]. Here, the gap between the functional layer and the silicon wafer is 2.5-μm. In another study [30], the gap was 0.6-μm with the supporting diaphragm thickness of 0.9-μm for the uncooled IR bolometric detector arrays. Drawbacks of surface micromachining are stress in the structure film, and possible sticking of the structures to the substrate [31]. These problems are especially critical in the application of tactile sensors like the fingerprint captures.

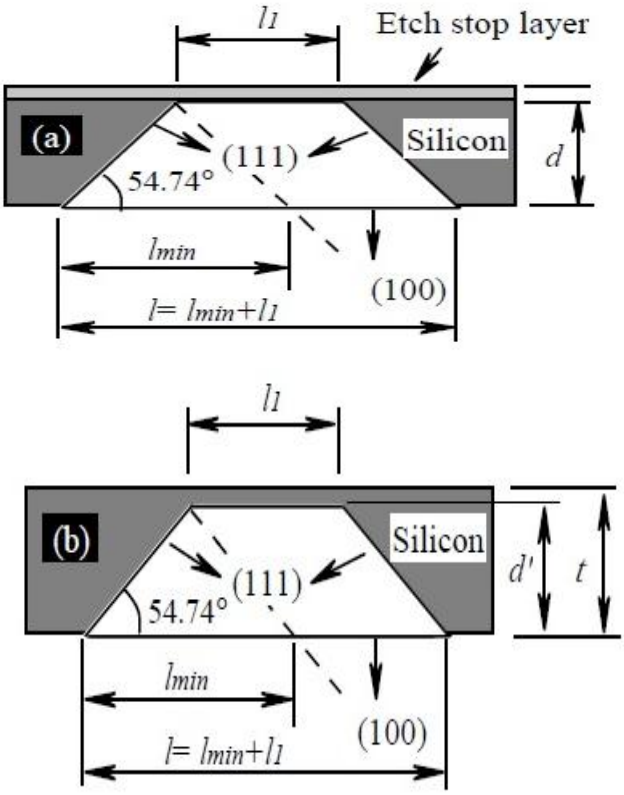

Fig. 2 Size reduction limited by anisotropic etching constraints: (a) Etching is controlled by etch-stop layer, and (b) Etching is controlled by etching time.

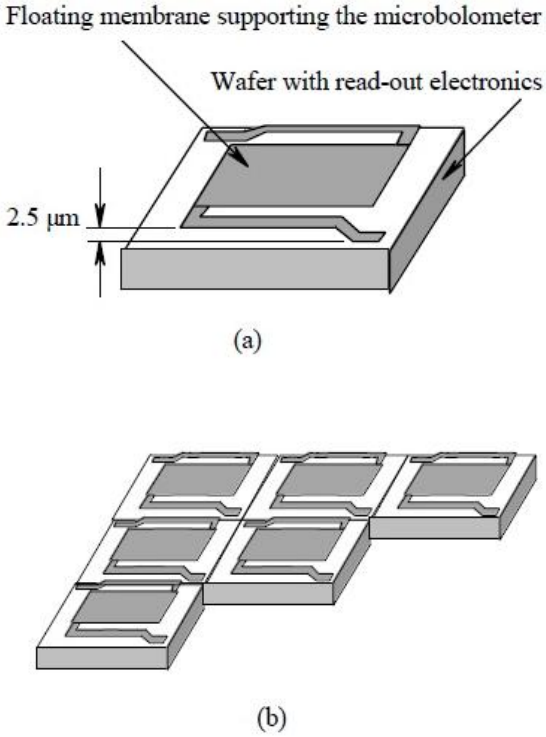

Fig. 3 Element structure of a matrix thermal sensor array by surface micromachining. This structure was developed at Honeywell, USA and applied for designing uncooled focal plane arrays [29]: (a) Single element, and (b) Arrayed elements image.

TABLE I. SOME REALIZED THERMAL SENSORS FROM PREVIOUS RESEARCHES

Ref.	Element number and arrangement	Elemet size (square μm)	Micromachining technology of thermal structure	Type of thermal structure	Material of thremal structure	Transducer principle	Transducer material	Application
[28]	32 linear staggered	800 ×400	bulk back-side	closed membrane	SiO_2/Si_3N_4	thermoelectric	poly-Si/Au	Infrared sensing
[32]	8 linear	3000 ×440	bulk fron-tside	cantilever beam	n-Si	thermoelectric	doped Si	Infrared sensing
[33]	16 linear staggered	2000 ×600	bulk back-side	closed membrane	SiO_2/Si_3N_4	thermoelectric	$Bi_{0.87}Sb_{0.13}/Sb$	Infrared sensing
[34]	4 linear	600 ×500	bulk front-side	bridge	SiO_2/Si_3N_4	thermoelectric	n/p poly-Si	Infrared sensing
[40]	64, 128, 256 linear	50 ×50 100 ×100	bulk front-side	floating membrane	Si_3N_4	thermoresistive	VO_2	Uncooled IR bolometer
[35]	32 ×32	375 ×375	bulk front-side, bulk back-side	closed membrane	SiO_2/Si_3N_4	thermoelectric	n/p poly-Si	Uncooled IR imager
[29]	340 ×240	50 ×50	surface	floating membrane	Si_3N_4	thermoresistive	VOx	Thermal imaging
[30]	64 ×64 128 ×128	50 ×50 100 ×100	surface	floating membrane	Si_3N_4	thermoresistive	VO_2	Uncooled IR bolometer
[36]	10 linear	40 ×40	surface	floating membrane bridge	SiO_2	thermoresistive	YBaCuO (semicond.)	Bolometer
[37]	128 ×128	100 ×100	surface	closed membrane	SiO_2	thermoelectric	n/p poly-Si	Uncooled IR focal plane
[38]	256 ×256	40 ×40	surface	floating membrane	Si_3N_4	thermoresistive	VO_2, doped Si	Infrared sensing
[39]	128 ×128	50 ×50	surface	floating membrane	SiO_2	thermoresistive	Ti	IR bolometer

Comparing to the surface micromachining, bulk micromachining technology is a well-established and understood technology, provides a reliable industrial process and requires only a small investment for the etching equipment. Further, by bulk micromachining, the problem of sticking between the diaphragm and the substrate can be avoided. Table I summarizes some realized thermal sensor arrays from the previous researches.

III. THERMAL ANALYSIS

A. *Electrical-thermal analogies*

The behavior of heat flow and temperature in thermal systems can be described mathematically by the same equations as those used for the electrical currents and voltages in electrical systems. The important advantage of this analogy is that it is convenient because of the advanced description and analysis tools available for electrical circuits, thus allowing a good overview of even very complex systems. Analogous to the electrical resistance (the ratio of the voltage difference over a structure and the resulting electrical current through it), it is possible to define the thermal resistance R_{th} as the ratio of the temperature difference ΔT and the heat flow P that causes the temperature difference, when the heat flow is in the steady-state situation:

$$R_{th} = \Delta T/P \qquad (1)$$

The thermal resistance has unit of KW^{-1}. The reciprocal of the thermal resistance is the thermal conductance G (in WK^{-1}).

Analogous to the electrical capacity, the thermal capacity of a body is defined as the ratio of the increase in the amount of energy that is stored and the resulting temperature rise. For a solid body of mass m and volume V, the thermal capacitance is given by:

$$C_{th} = cm = c\rho V \qquad (2)$$

Where, c (in J kg^{-1} K^{-1}) is the specific heat at a constant pressure and ρ (in kg m^{-3}) the density of the body. The electrical equivalents of thermal parameters are listed in Table II together with the SI units in which they are expressed.

TABLE II. ELECTRICAL EQUIVALENTS OF THERMAL PARAMETERS

Thermal parameter	Electrical parameter
Temperature: T (K)	Voltage: V (V)
Heat flow, power: P (W)	Current: I (A)
Heat: Q (J=W s)	Charge: Q(C= A s)
Resistance: R (K W^{-1})	Resistance: R (Ω= V A^{-1})
Conductance: G (W K^{-1})	Conductance: G (Ω^{-1})
Capacity: C (J K^{-1})	Capacitance: C (F= A s V^{-1})
Thermal resistivity: ρ_{th} (K m W^{-1})	Electrical resistivity: ρ_{el} (Ω m)
Thermal conductivity: λ (W m^{-1} K^{-1})	Electrical conductivity: σ (Ω^{-1} m^{-1})
Specific heat: c_p (J kg^{-1} K^{-1})	Permittivity or capacitivity: ε(F m^{-1})

B. Sensing-element models

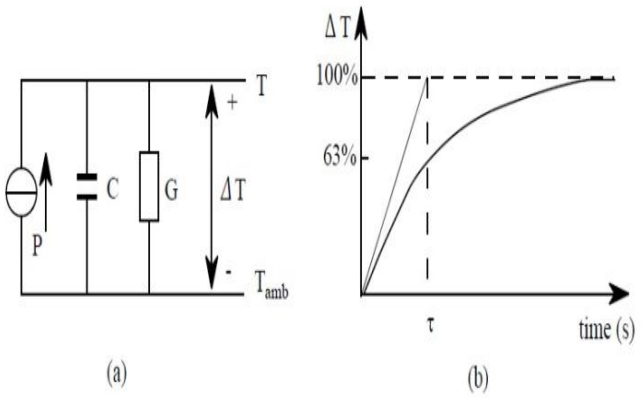

Fig. 4 Single-element model of a thermal sensor: (a) electrical circuit, and (b) step response curve for a first-order circuit.

When the details of the temperature distribution inside the body are of no interest, the thermal behavior is sufficiently described by the heat balance for the entire body (lumped-element model):

$$C\,(d\Delta T/dt) = P - G(T - T_{amb}) = P - G\Delta T \qquad (3)$$

Where, C is thermal capacity of the body, G the thermal conductance representing the heat transfer to the ambient, and P the amount of power generated in the body. The temperature T and T_{amb} refer to those of the body and the ambient, respectively. The electrical equivalent circuit is shown in Fig. 4-a. In the steady-state situation the temperature rise in the sensor above the ambient which results from the power dissipation P is equal to $\Delta T = T - T_{amb} = P/G$. The time response of the system, when the heating power is abruptly changed from zero to a constant value P_0 at time t =0, and when it is assumed that the sensor is initially at the ambient temperature (ΔT =0) and all other components in the circuit are chosen to be linear and constant in time, is given by:

$$\Delta T(t) = P/G\,(1-exp(-t/\tau)) \qquad (4)$$

$$\tau = C/G \qquad (5)$$

Where, the time constant (or response time) τ, is defined as the time for the signal to reach 63% of its final value (Fig. 4-b). A similar result can be found when an abrupt change in T_{amb} or in G is taken into consideration. The thermal impedance $Z=\Delta T/P$ for a sinusoidal variation of P with radial frequency ω (rad s^{-1}) follows from basic circuit theory (where $R = G^{-1}$):

$$Z(\omega) = (G + j\omega C)^{-1} = R\,(1+j\omega RC)^{-1} \qquad (6)$$

The above expression is for a first-order RC circuit with time constant $\tau = RC$. In thermal sensors, it is important to realize larger temperature rise with a fast response under little input power. For a fast response, a smaller time constant is necessary. In order to minimize τ, it is required to minimize C and enlarge G. But, by enlarging G, ΔT will be reduced. From equations (4) and (5), it can be understood that in order to obtain a small τ and a large ΔT at the same time, there is only one method, i.e. minimize G and minimize C further. For minimizing C, it is necessary to miniaturize the heater element. The floating type air-bridge structure is useful for this purpose. For minimizing G, the heat-loss to the substrate (including the wiring) needs to be as small as possible.

C. Thermal analysis by simulation

Thermal analysis was performed by simulation employing the FUJITSU/α-FLOW software package. When the sensor structure and dimensions are decided, the 3-D problems of the heat transfer can be solved by inputting the input power P (W), during time τ (ms) as well as the ambient temperature T, and the sensor component's material properties including thermal conductivity λ ($Wm^{-1}K^{-1}$), heat capacity c ($J\,kg^{-1}K^{-1}$) and density ρ ($kg\,m^{-3}$). Following heat conduction equation was used in calculation:

$$\rho c \frac{\partial T}{\partial t} = \lambda\left(\frac{\partial^2 T}{\partial x^2} + \frac{\partial^2 T}{\partial y^2} + \frac{\partial^2 T}{\partial z^2}\right) + \dot{Q} + q \qquad (7)$$

Where, $\dot{Q}$ is the generated heat in per unit volume and per unit time, and q is the heat transfer by. Considering fingerprint sensor application, q was ignored in this calculation.

1. Simulation model

We supposed the most severe situation in thermal sensor like fingerprint capture as the simulation model. The proposed thermal type micro fingerprint sensor, has arrayed high density micro heater elements. To provide thermal isolation, the substrate has to be made of a less heat conductive material, and when necessary, thermal insulation layers should be arranged under the heater elements to reduce the heat transfer to the substrate. When a fingertip is pressed on the sensor surface, the heater elements in contact with a fingerprint ridge, e.g., E_1, will show a smaller temperature rise than the elements facing a fingerprint valley, e.g., E_2, because of the difference in the thermal path between the two conditions. The ridges act as heat sinks, while the valleys act as thermal insulators due to the air in the valley. When a pulsed voltage is applied to each heater element, element E_1 will show a smaller temperature rise than element E_2. The temperature-rise differences between the heater elements underneath the ridges and valleys of the fingerprint can be used to reconstruct and display an image of the fingerprint patterns by means of the circuit technology.

In order to simplify the calculation, the following conditions are supposed:

- Heat transfer by radiation is ignored;
- Fingertip is directly in contact with every heater element, and there are no fluid flow including the air in the valley of the fingerprint;
- Heater elements are two-dimensionally arrayed;
- Boundary condition at the sidewall of each sensor element is same to each other due to the structural symmetry.

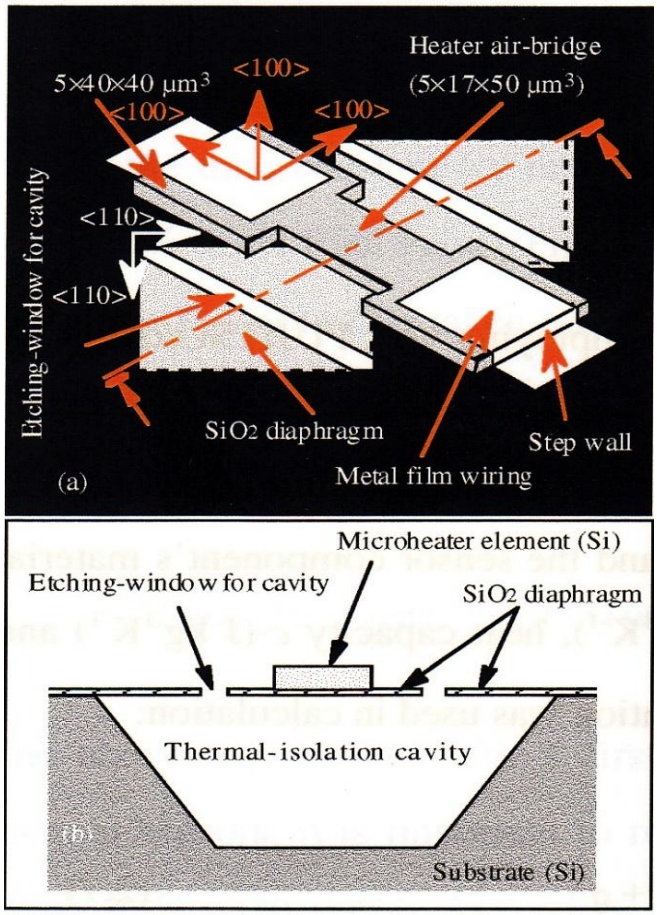

Fig. 5 Fingerprint sensor model for the simulation calculation: (A) Proposed sensor structure with SOI (silicon on insulator) wafer as the starting material for real fabrication (a: top view, b: cross-sectional view); (B) Simulation model structure used in calculation (basic size got from Fig. A).

The structure and dimension of the basic model is shown in Fig. 5. Because of the structural symmetry, only a quarter of the sensor element was used in simulation for the shorter of calculation time. For the real device design, thermal analysis was performed by simulation using this model changing the structural component (including insulation layer, cavity) and the size as well as material property of the components.

2. SiO_2 layer effect

The thermal isolation effect of a 1-μm-thick silicon dioxide for the sensor sensitivity was examined comparing with non-SiO_2 layer structure as shown in Fig. 6 shows. Input power was 50mW/1.0ms. By 1-μm thick SiO_2 layer, 10°C higher of temperature rise was obtained on the heater element. By increasing the SiO_2 layer to the thickness of 2-μm, another 10°C of temperature rise was realized as shown in Fig. 7. SiO_2 layer can result in an effective thermal insulation. Nevertheless, in the real fabrication process, to produce a thicker of SiO_2 layer (>2-μm) will be time consuming and not a cost-effective solution.

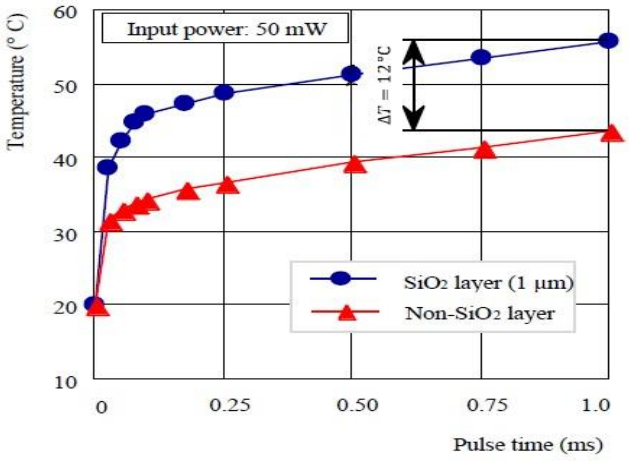

Fig. 6 Silicon dioxide layer effect to the thermal isolation

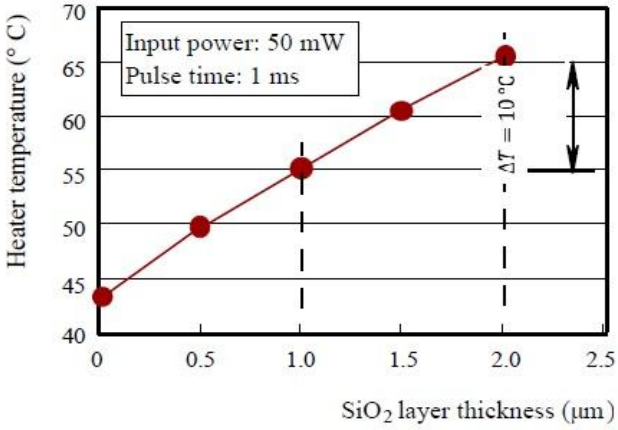

Fig. 7 Thickness effect of SiO_2 layer to the thermal isolation.

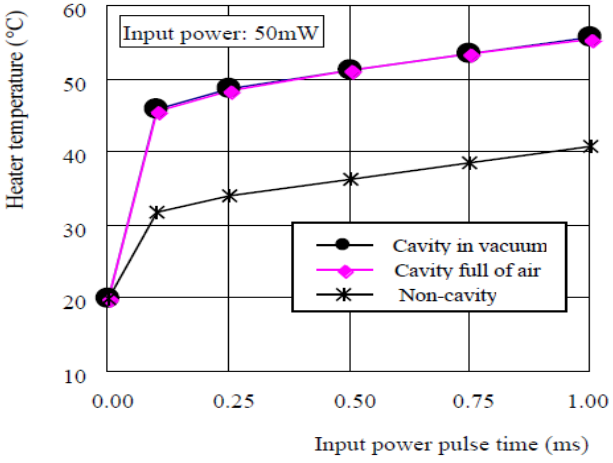

Fig. 8 Cavity effect to the thermal isolation results.

3. Cavity effect

Figure 8 shows the cavity effect to the thermal isolation. About 14°C of temperature rise is achieved at the input power of 50mW. However, there is almost no temperature change between the following two situations: the cavity is in full of air and in a vacuum. It means, in cavity the heat transfer by convection of the air is very small and can be ignored. To make the thermal isolation further, broaden cavity will be efficient than the deeper one.

4. Heater size and material effects

In Fig. 9, effects of the heater size and its material selection to the sensor sensitivity are evaluated. Silicon and platinum are selected as the heater material for comparing. Thickness of 5-μm and 0.5-μm are used in the silicon heater. Under the input power 50mW, about 80°C more of the temperature rise was obtained on the 0.5-μm thick silicon heater element, comparing to that of 5-μm one, due to the smaller thermal capacity. Under the same input power, another 80°C more of the temperature rise was achieved on the heater element by using 0.5-μm thick platinum instead of 0.5-μm thick silicon. It is attributed by the platinum material properties of smaller thermal conductivity [$Wm^{-1}K^{-1}$] (Si:150, Pt:73) and smaller specific heat *Cp* [J $kg^{-1}K^{-1}$] (Si:702, Pt:132.5). At the same size, heater material having smaller value of thermal conductivity and specific heat is a better choice in thermal sensor.

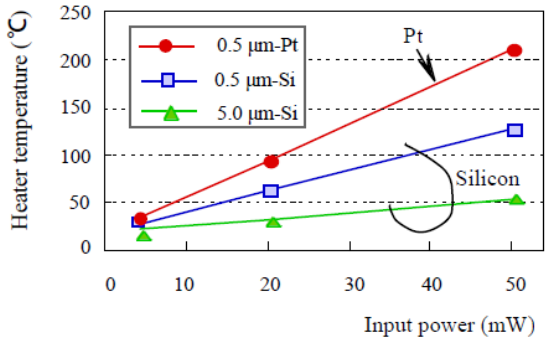

Fig. 9 Heater size and material effect (τ=1ms)

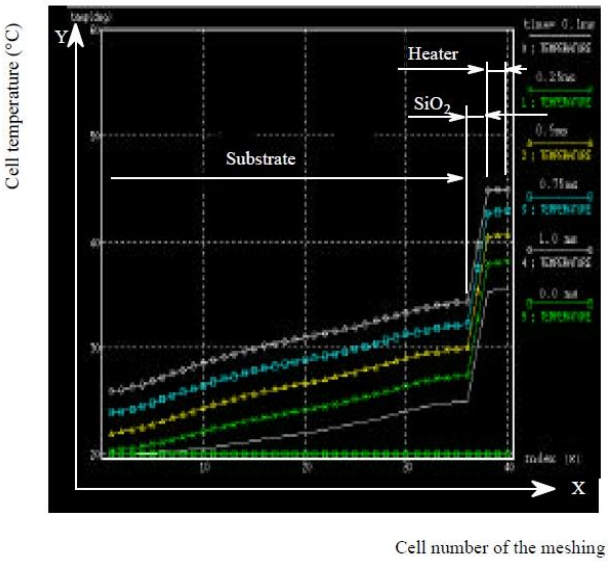

Fig. 10 Temperature distribution on the supporting pad of the heater at the thickness direction.

5. Temperature distribution

The heat loss from supporting pad (see Fig. 5) to the silicon substrate was investigated. Figure 10 shows the temperature distribution from the point B in supporting pad to the substrate in thickness direction. X-axis shows the cell number of the meshing in the thickness direction and Y-axis is the cell temperature at every position. Different colors of graphs correspond to the state of different moments during the input power time of 0~1ms. SiO_2 layer results in a big temperature gradient.

6. Transferred heat ratio in each component

By the FUKITSU/α-FLOW software package, it is possible to evaluate the temperature distribution at every moment but cannot directly understand the transferred heat ratio in every component. Using the following equations, further analysis was possible based on the simulation results.

$$\emptyset_t = \lambda \frac{\delta T}{\delta n} \quad (8)$$

Where, λ shows thermal conductivity [$Wm^{-1}K^{-1}$] and $\emptyset_t$ [Wm^{-2}] the heat flux on every cell of the heater surface at the moment *t*.

$$q_t = \int_S \emptyset_t dS \quad (9)$$

Where, q_t [W] shows the amount of heat transfer through the heater surface *S* at the moment *t*.

$$Q_{t0} = \int_0^{t_0} q_t dt \quad (10)$$

Where, Q_{t0} [J] shows the total amount of heat through the heater surface *S* during the time of $0 \sim t_0$.

$$Q = P \times \tau \quad (11)$$

Where, *Q* is the total amount of the heat [J], *P* is the input power [W], and τ [s] is during time of the input power.

$$Q = \sum_{x=1}^{m} Q_x \quad (12)$$

Where, *m* shows the number of sensor components for example heater element, isolation membrane and substrate, and the subscript *x* refers to one of the any component.

$$Q_x = \sum_{i=1}^{n} \{\rho_x \times c_x \times V_{xi} \times (T_{xi} - T_0)\} \quad (13)$$

Where, *n* shows the meshed cell number in every component, and the subscript *i* refer to one of the any cell in every component. In addition, ρ shows the density [kgm^{-3}], *c* the specific heat [J kg^{-1} K^{-1}], *V* the volume of component, T_{xi} the cell temperature of every component [K], and T_0 the ambient temperature [K].

$$Q_{xr} = \left(\frac{Q_x}{Q}\right) \times 100\% \quad (14)$$

Where, the subscript *r* refers to the heat ratio of every component to the total heat generated in the heater.

$$T_{x(mean)} = \sum_{i=1}^{n} (V_{xi} \times T_{xi}) / V_x \quad (15)$$

Where, $T_{x(mean)}$ shows the mean temperature of every component. At the condition of 150mW input power and 3ms of moment time, the calculated heat rate consumed in every component is shown in Table III. Most of the input power is consumed in the substrate. Here, the material properties of the fingertip that necessary in simulation calculation are used as leather and air [Data from reference 41]. Leather: thermal conductivity λ: 0.15 (W $m^{-1}K^{-1}$), heat capacity c : 1.5 (J $kg^{-1}K^{-1}$), and density ρ: 1.0 (kg m^{-3}).

7. Material property effects

Selection of the substrate and the heater material is an important point in the applicable sensor design. In order to understand the effects of their material properties to the sensor sensitivity, the author evaluated the effects of the substrate and the heater by varying their thermal conductivity λ ($Wm^{-1}K^{-1}$), heat capacity c (J $kg^{-1}K^{-1}$) and density ρ (kg m^{-3}). Figure 11 shows the simulation results about the effects of substrate and heater's material properties to the thermal isolation at the structure condition of 400-μm thick substrate and 5-μm thick heater with 1-μm thick SiO_2 layer. Input power is 50mW and input power during time is 1ms. In Fig. 11, (a) is the effect of thermal conductivity, (b) is that of density and (c) is that of specific heat. Form Fig. 11, it is known that varying the parameters of heater material properties is not so sensitive to the heater temperature comparing to that of the substrate. Furthermore, when varying the material properties of substrate, thermal conductivity is the most sensitive parameter. It means that, at the condition of the same structure, to change thermal conductivity of the substrate is an efficient way for the desired thermal isolation. In Table IV, thermal properties of some commonly used materials are summarized.

TABLE III. CONSUMED HEAT RATE IN EVERY COMPONENT

Heat rate [%] / Fingertip contacting	Q_{heater} [%]	Q_{SiO_2} [%]	$Q_{substrate}$ [%]	$Q_{fingertip}$ [%]
Finger ridge-contacting	0.87	0.35	82.41	16.36
Finger valley-contacting	1.05	0.45	98.48	0.02

(input power: 150-mW, time duration: 3-ms)

TABLE IV. COMPARING OF MATERIAL PROPERTIES (DATA FROM [41-44])

Material / Parameter	Silicon	SiO_2	Si_3N_4	Polyimide film		Pt	Ni	Cu
				Kapton	Upilex			
λ (W m^{-1} K^{-1})	150	1.4-11	16-33	0.12	0.29	73	59	384
ρ (g cm^{-3})	2.3	2.2	3.4	1.42	1.47	21.4	8.9	8.9
C (J kg^{-1} K^{-1})	702	840	710	1130	1090	132.5	461	394

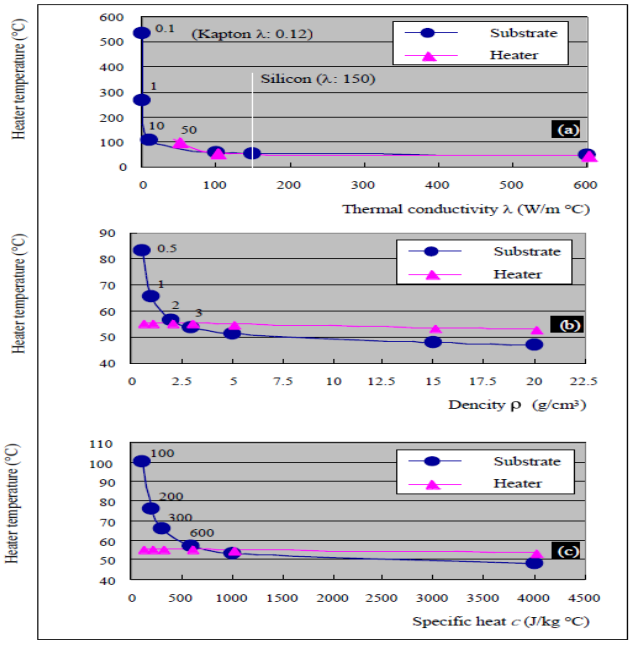

Fig. 11 Effects of substrate and heater's material properties to the sensor sensitivity at the dimensional condition of 400-μm thick substrate and 5-μm thick heater with 1-μm thick SiO_2 layer. Input power is 50mW and input power during time is 1ms: (a) effect of thermal conductivity; (b) effect of density; and (c) effect of specific heat.

IV. MECHANICAL STRENGTH ANALYSIS BY SIMULATION

The sensor structure must have enough mechanical strength, because of the unavoidable contacting pressure in the particular application of a fingerprint sensor. Human fingertip pressure on the fingerprint sensor surface is supposed to be 1kg/cm^2. To investigate mechanical strength of the structure, the Finite Element Method (FEM) was used employing the I-DEAS software package. Figure 12 shows the simulation results. The sensor dimensions and the geometrical shape are from Fig. 5-(A). Figure 12-a show the created FE model with a uniform load of 1kgf/cm^2 on the heater element (silicon air-bridge) and the SiO_2 diaphragm. Underneath the heater element is a cavity isolated from the heater element by the 1-μm thick SiO_2 diaphragm. Figure 12-b shows the used mesh. Fine meshes are taken in the area of the air-bridge in order to investigate detail information about the stress concentration. Figure 12-c shows the calculation results. The maximum stress on the sensor element reached 2.59×10^5 mN/mm^2. Because the yield strength of silicon and SiO_2 is 7.0×10^6 and 8.4×10^6 mN/mm^2, respectively (data from the "MEMS Material Database" [42]), it is clear that the proposed structure has enough mechanical strength.

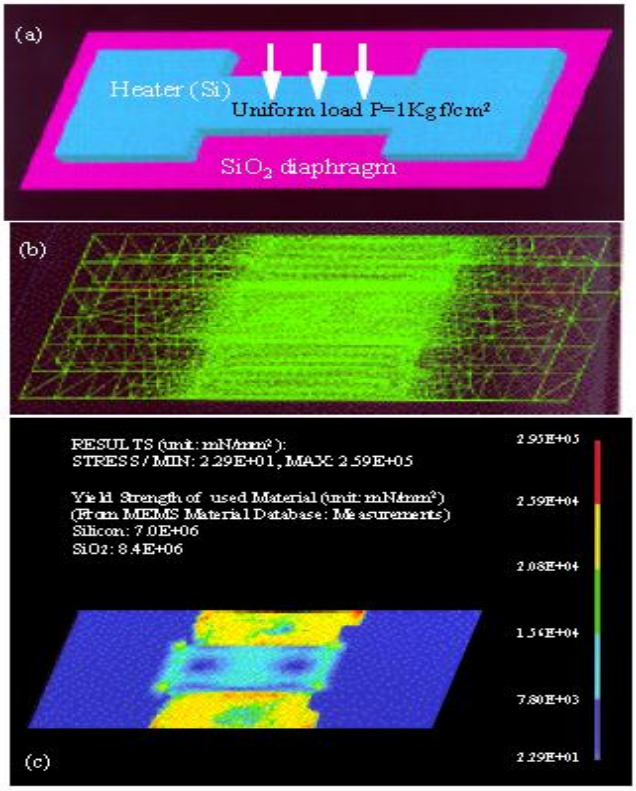

Fig. 12 Mechanical strength analysis by I-DEAS: (a) simulation model; (b) meshed state for calculation, and (c) calculation results by simulation.

In order to evaluate the sensor properties experimentally, prototype is fabricated to realize the target structure of Fig. 5-(A) as shown in Fig. 13. In the prototype, a p-type (100) SOI wafer was used as the starting material.

The model and analysis by simulation in this paper was performed using the most severe situation of fingerprint capture as the example. For the limit to the number of page, the evaluation by experimental results and the polymer based approach will be reported in another paper "Structural design points in arrayed micro thermal sensors (II) ~ Experimental verification ~ ".

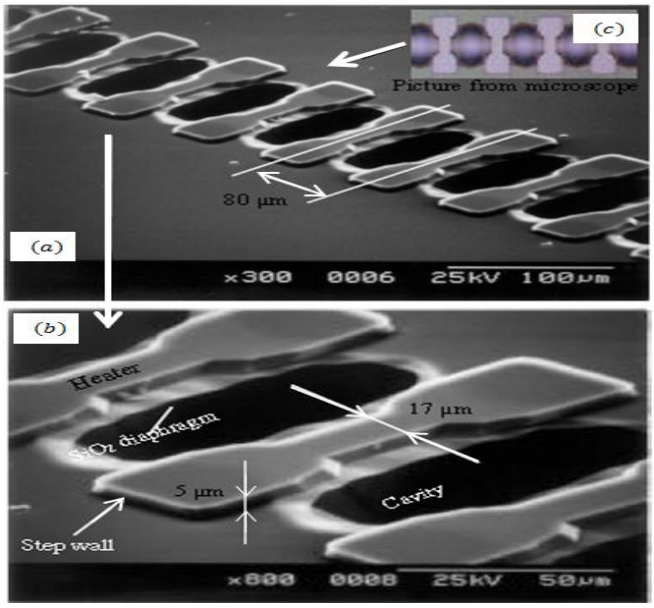

Fig. 13 SEM picture of the first prototype: (a) arrayed micro heater elements consisting of a diaphragm and a laterally interpenetrated cavity under each element; (b) enlarged view of (a), and (c) optical microscopy image of (a).

V. SUMMARY

Design points of single and arrayed micro thermal sensor structures are discussed including its fabrication process technology. Approach of electrical-thermal analogies is applied to analyze the effects of the sensor structure as well as the composed material properties to the thermal characteristic of the sensor by simulation. In this paper the simulation analysis was performed using the model that associated with the most severe situation of fingerprint capture as the example.

By simulation, the following features were become clear:

(1). SiO_2 layer can result in a big temperature gradient, and the insulation effect shows linear increase with its thickness by 10 °C/μm thermal isolation results.

(2). 40-μm depth of cavity under the heater element acts as a good insulation layer. The heat transfer by convection of the air in the cavity is negligible, and there is almost no difference in the isolation effects between air and vacuum in the cavity. So, for the purpose of further thermal isolation, broaden cavity will be more efficient than the deeper one.

(3). Thermal capacity of the heater element need to be as small as possible for the heat loss and thermal response. Under the input power 50mW, over 80°C of the temperature rise was obtained on the 0.5-μm thick silicon heater element, comparing to that of 5-μm one, due to the smaller thermal capacity.

(4). Heater element material properties such as thermal conductivity and specific heat as well as density need to be as small as possible. Under the same input power, another 80°C more of the temperature rise was achieved on the heater element by using 0.5-μm thick platinum instead of 0.5-μm thick silicon. It is attributed by the platinum material properties of smaller thermal conductivity [$Wm^{-1}K^{-1}$] (Si: 150, Pt: 73) and smaller specific heat *Cp* [$J\ kg^{-1}K^{-1}$] (Si: 702, Pt: 132.5).

(5). Proposed structure of the fingerprint capture with a 5-μm tick silicon heater-bridge and 1-μm thick SiO_2 diaphragm have enough strength to the fingertip pressure (>10 N/cm^2).

(6). Over 80 % of the input power was consumed at the substrate. Thermal conductivity of the substrate is the most sensitive parameter and the idea of thermal isolation from the heater element to the substrate is the most important key point in the structural design to realize a high resolution and sensitive micro thermal sensor.

Further of the results based on the experimental verification in silicon-based approach and the results of polymer based approach will be reported in another paper soon.

REFERENCES

[1] Venkatarman Chandrasekaran, Anthony Cain, Toshikazu Nishida, louis N. Cattafesta and Mark Sheplak, Characterization of a micromachined thermal shear stress sensor, 39th Aerospace Sciences Meeting & Exhibit, 8-11 Jan. 2001/Reno, NV, AIAA 2001-2047.

[2] O. Tabata, Fast-response silicon flow sensor with an on-chip fluid temperature sensing element, IEEE Trans. Electron Devices, ED-33 (1986) 361-365.

[3] O. Tabata, H. Inagaki and I. Igarashi, Monolithic pressure-flow sensor, IEEE Trans. Electron Devices, ED-34 (1987) 2456-2462.

[4] E. Yoon and K. D. Wise, A dielectrically-supported multi-element mass flow sensor, IEEE IEDM Tech. Digest, 1988, 670-673.

[5] S. Bouwstra, P. Kemna and R. Legtenberg, Thermally exited resonating membrane mass flow sensor, Sensors and Actuators, 20 (1989) 213-223.

[6] Carole Rossi, Emmanuel Scheid, Daniel Estéve, Theoretical and experimental study of silicon micromachined microheater with dielectric stacked membranes, Sensor and Actuators A 63 (1997) 183-189.

[7] F. Solzabacher, C. Imawan, H. Steffes, E. Obermeier, A new low power SiC/HfB2-based microhotplate with integrated IDC for metal oxide gas sensors, Proceedings of the Transducers'99, Sendai, Japan, 1999, 1032-1035.

[8] P. Maccagani, L. Dori, P. Negrini, Eurosensors XIII, the 13th European Conference on Solid-State Transducers September 12-15, 1999, The Hague, The Netherlands, Thermo-insulated microstructures based on thick porous silicon membranes, 817-820.

[9] I. Simon, M. Arndt, Thermal and gas-sensing properties of a micromachined thermal conductivity sensor, in: Proceedings of the Transducers'01 Eurosensors, Vol. XV, 2001, 1492-1495.

[10] Kwang-hyun Lee, Hyung-kew Lee, Hee-jin Byun, Il-Joo Cho, Jong-uk Bu, Euisik Yoon, An audio frequency filter application of micromachined thermally-isolated diaphragm structures, Sensors and Actuators A 89 (2001) 49-55.

[11] Y. C. Tai and R. S. Muller, Lightly-doped polysilicon bridge as a flow meter, Sensors and Actuators, 15 (1988) 63-75.

[12] K. Petersen, J. Brown and W. Renken, High-precision, high-performance mass-flow sensor with integrated laminar flow micro-channels, in: Proceedings of the 3rd Int. Conf. Solid-State Sensors and Actuators (Transducers'85), Philadelphia, PA, U.S.A., June 7-11, 1985, 361-363.

[13] R. G. Johnson and R. E. Higashi, A highly sensitive silicon chip microtransducer for air flow and differential pressure sensing applications, Sensors and Actuators, 11 (1987) 63-72.

[14] M. Esashi, S. Eoh, T. Matsuo and S. Choi, The fabricaion of integrated mass flow controllers, in: Proceedings of the 4th Int. Conf. Solid-State Sensors and Actuators (Transducers'87), Tokyo, Japan, June 2-5, 1987, 830-833.

[15] S. Bouwstra, R. Legtenberg, H. A. C. Tilmans and M. Elwenspoek, Resonating microbridge mass flow sensor, Sensors and Actuators, A21-A23 (1990) 332-335.

[16] M. Kimura, M. Yoshida and N. Suzuki, Schottky barrier thermistor on the micro-air-bridge, in: Proceedings of the 7th International Conference on Solid-State Sensors and Actuators Transducers'93, June 7-10, 1993, Pacifico, Yokohama, Japan, 746-749.

[17] Mitsuteru, Kimura, Junji Manaka, Shigemasa Satoh, Shigeki Takano, Norikazu Igarashi, Kazutoshi Nagai, Application of the air-bridge microheater to gas detection, Sensors and Actuators B 24-25 (1995) 857-860.

[18] Takudai Neda, Kenichi Nakamura, Tsugihiko Takumi, A polisilicon flow sensor for gas flow meters, Sensors and Actuators A54 (1996) 626-631.

[19] J.-I. Hayasaka, C. Sawai, M. Kimura, Study on ultraminiature thermal analysis device with micro-air-bridge heater and new method for its heating-rate curve, T. IEE, Vol. 119E, No. 3, Japan, 1999, 119-124.

[20] G. N. Stemme, A monolithic gas flow sensor with polyimide as thermal insulator, IEEE Trans. Electron Devices, ED-33 (1986) 1470-1474.

[21] L. Löfdahl, G. Stemme and B. Johansson, A sensor based on silicon technology fo turbulence measurements, J. Phys. E: Sci. Instrum., 22 (1989) 391-393.

[22] B. W. van Oudheusden and A. W. van Herwaarden, High-sensitivity 2-D flow sensor with an etched thermal isolation structure, Sensors and Actuators, A21-A23 (1990) 425-430.

[23] B. H. Kim, F. E. Prins, D. P. Kern, S. Raible, U. Weimar, Multicomponent analysis and prediction with a cantilever array based gas sensor, Sensors and Actuatore B 78 (2001) 12-18.

[24] M. Parameswaran, A. M. Robinson, Lj. Ristic, K. Chau and W. Allegretto, A CMOS thermally isolated gas flow sensor, Sensors Mater., 2 (1990) 17-26.

[25] D. Moser, R. Lenggenhager and H. Baltes, Silicon gas flow sensors using industrial CMOS and bipolar IC technology, Sensors and Actuators A, 25-27 (1991) 577-581.

[26] Shih-Ta hung, Shwin-Chung Wong, Weileun Fang, The development and application of microthermal sensors with a mesh-membrane supporting structure, Sensors and Actuators 84 (2000) 70-75.

[27] Mitsuhiko nagata, Malcolm Stevens, Nicholas Swart, Thangaraj Dravia, Arokia Nathan, Optimization of two-element flow microsensors using quasi 3-D numerical electrothermal analysis, Sensors and Actuators A 90 (2001) 102-110.

[28] I. H. Choi, K. D. Wise, A silicon-thermopile-based infrared sensing array for use in automated manufacturing, IEEE Trans. On Electron Devices, ED-33 (1986) 72-79.

[29] R. A. Wood, Uncooled thermal imaging with monolithic silicon focal planes, Proc. SPIE, 2020 (1993) 322-329.

[30] H. Jerominek, M. Renaud, N. R. Swart, F. Picard, T. D. Pope, M. Levesque, M. Lehoux, G. Bilodeau, M. Pelletier, D. Audet, P. Lambert, Micromachined VO2-based uncooled IR bolometric detector arrays with integrated CMOS readout electronics, Proc. SPIE, 2882 (1996) 111-121.

[31] U. Dillner, Thermal simulation and realization of micromachined thermal sensor arrays, Proceedings of 5th NEXUSPAN Workshop on Thermal Aspects in Microsystem Technology (Invited Paper), Budapest, 1998, 133-141.

[32] P. M. Sarro, H. Yashiro, A. W. V. Herwaarden, S. Middelhoek, An integrated thermal infrared sensing array, Sensors and Actuators, 14 (1988) 191-201.

[33] W. Schnelle, U. Dillner, S. poster, A linear thermopile infrared sensing array, VDI-Berichte, 982, (1992) 261-264.

[34] R. Lenggenhager, H. Baltes, T. Elbel, Thermoelectric infrared sensors in CMOS technology, Sensors and Actuators, A37-38 (1993) 216-220.

[35] A. D. Oliver, W. G. Baer, K. D. Wise, A bulk-micormachined 1024-element uncooled infrared imager, Transducers'95 Digest of Technical Papers, Vol. 2, Stockholm, 1995, 636-639.

[36] C. M. Travers, A. Jahanzeb, D. P. Butler, Z. Celik-Butler, Fabrication of semiconducting YbaCuO surface-micromachined bolometer arrays, J. Microelectromech. Systems, 6 (1997) 271-276.

[37] T. Kanno, M. Saga, S. Matsumoto, M. Uchida, N. Tsukamoto, A. Tanaka, S. Itoh, A. Nakazato, T. Endoh, S. Tohyama, Y. Yamamoto, S. Murashima, N. Fujimoto, N. Teranishi, Uncooled infrared focal plane array having 128´128 thermopile detector elements, Proc. SPIE, 2269 (1994) 450-459.

[38] K. C. Liddiard, M. H. Unewisse, O. Reinhold, Design and fabrication of thin film monolithic uncooled infrared detector arrays, Proc. SPIE, 2225 (1994) 62-71.

[39] A. Tanaka, S. Matsumoto, N. Tsukamoto, S. Itoh, T. Endoh, A. Nakazato, Y. Kumazawa, M. Hijikawah, H. Gotoh, T. tanaka, N. Teranashi, Silicon IC process compatible bolometerinfrared focal plane array, Transducers'95 Digest of Technical papers, Vol. 2, Stockholm, 1995, 632-635.

[40] H. Jerminek, F. Picard, N. R. Swart, M. Renaud, M. Levesque, M. Lehoux, J. S. Castonguay, M. Pelletier, G. Bilodeau, D. Audet, T. D. Pope, P. Lambert, Micromachined, uncooled, VO2-based IR bolometer arrays, Proc. SPIE, 2746 (1996) 60-71.

[41] Kurt Gieck, Technische Formelsammlung, Jan. 1987, translated by Ohda Hiroshi.

[42] "MEMS Material Database: Measurements", http://mems.isi.edu/mems/materials/measurements.cgi

[43] Catalogue, Kapton Polyimide film, Du Pont-Toray Co., ltd., Japan.
Catalogue, Upilex Polyimide film, Ube Industries, Ltd., Japan